Defense Technical Information Center
Compilation Part Notice

ADPO14183

TITLE: The Dependence of Store-Induced Limit-Cycle Oscillation
Predictions on Modelling Fidelity

DISTRIBUTION: Approved for public release, distribution unlimited
Availability: Hard copy only.

This paper is part of the following report:

TITLE: Reduction of Military Vehicle Acquisition Time and Cost through
Advanced Modelling and Virtual Simulation [La reduction des couts et des
delais d'acquisition des vehicules militaires par la modelisation avancee et
la simulation de produit virtuel]

To order the complete compilation report, use: ADA415759

The component part is provided here to allow users access to individually authored sections
of proceedings, annals, symposia, etc. However, the component should be considered within
the context of the overall compilation report and not as a stand-alone technical report.

The following component part numbers comprise the compilation report:
ADPO14142 thru ADPO14198

The Dependence of Store-Induced Limit-Cycle Oscillation Predictions on Modelling Fidelity

P.S. Beran, N.S. Khot, F.E. Eastep, R.D. Snyder, J.V. Zweber, L.J. Huttsell, J.N. Scott
Multidisciplinary Technologies Center
Air Force Research Laboratory (AFRL), Air Vehicles Directorate
AFRL/VASD, 2210 Eighth Street, Building 146
Wright-Patterson AFB, Ohio, 45433
United States

Abstract

Store-induced limit-cycle oscillation of a rectangular wing with tip store in transonic flow is simulated using a variety of mathematical models for the flow field: transonic small-disturbance theory (with and without inclusion of store aerodynamics) and transonic small-disturbance theory with interactive boundary layer (without inclusion of store aerodynamics). For the conditions investigated, limit-cycle oscillations are observed to occur as a result of a subcritical Hopf bifurcation, and are obtained at speeds lower than those predicted (1) nonlinearly for clean-wing flutter, and (2) linearly for wing/store flutter. The ability of transonic small-disturbance theory to predict the occurrence and strength of this type of limit-cycle oscillation is compared for the different models. Solutions computed for the clean rectangular wing are compared to those computed with the Euler equations for a case of static aeroelastic behavior and for a case of forced, rigid-wing oscillation at Mach 0.92.

Nomenclature

α	angle of attack, degrees
c	chord, ft
cg, ea	center of gravity and elastic axis, ft from leading edge
C_L, C_M	lift and moment coefficients (moment about leading edge)
i, j, k	computational index coordinates
l	span, ft
M	Mach number
Re	Reynolds number (based on root chord)
ρ	density, slugs/ft^3
t	time, nondimensional (based on freestream velocity and wing chord)
T	temperature, °R
τ	thickness to chord ratio
U	velocity, ft/sec
x, y, z	physical coordinates (streamwise, spanwise, vertical), feet
ζ	structural damping coefficient, nondimensional

Subscripts

∞	freestream condition
s, w	store or wing property, respectively
o	wing root property

Introduction

High-performance fighter aircraft with external stores are required to operate with high manoeuvrability in the transonic flight regime. In this regime, the potential exists for encountering transonic nonlinear flutter, known as limit-cycle oscillation (LCO). LCO is a limited amplitude, self-sustaining oscillation produced by an aerodynamic-structural interaction, which for the cases of interest, is exasperated by the occurrence of shock waves on the surface of the wing and/or stores. LCO results in an undesirable airframe vibration and limits the performance of the flight vehicle.

The main goal of the current work is to determine the range of applicability of models of varying fidelity to the numerical prediction of store-induced LCO. This form of LCO typically occurs near linear flutter boundaries in the nonlinear, transonic regime (Mach number ranging between 0.8 and 1.1), suggesting that classical flutter predictions using linear aerodynamic theories can be applied to the identification of lightly damped modes that may nonlinearly participate in LCO. Indeed, using traditional approaches, Denegri (2000) had limited success in relating observed store-induced LCO to "hump" (or "soft" crossing) modes found in velocity-damping diagrams. However, in many cases, the linear approach is inadequate in predicting response characteristics of vehicle configurations in the transonic regime.

The transonic regime differs from the linear, subsonic regime by the appearance of shocks. These structures may strongly interact with vehicle boundary layers, with the possible consequences of flow separation or significant shock movement. Following advances in nonlinear modeling and computer hardware, nonlinear aeroelastic predictions, including viscous effects and manoeuvre loads, are tractable for reasonably complex configurations (Melville (2001, 2002), Farhat *et al.* (2000)). Still, the use of modeling techniques that account for viscosity is too computationally demanding for preliminary design. In a coordinated manner, we examine the ability of aeroelastic models of varying fidelity to predict accurately LCO onset and amplitude. Models based on linear analysis, transonic small-disturbance theory (TSDT), and TSDT with interactive boundary layer are considered. Through this approach, we discern: (1) the limitations of linear theory for LCO prediction vis-à-vis the simplest nonlinear theory capable of producing weak shocks; (2) the ability of TSDT to predict store-induced LCO in inviscid flow, and (3) the effects of viscosity on store-induced LCO. This work provides the increased understanding of the LCO phenomenon, while also serving to determine the range of applicability and computational cost of various modeling techniques to the prediction of this phenomenon.

Three computational methodologies are employed in this investigation: the MSC/NASTRAN aeroelastic analysis program, the TSDT-based NASA/LaRC CAPTSDv computational aeroelasticity algorithm for inviscid and viscous flow, and the AFRL ENS3DAE Euler/Navier-Stokes computational aeroelasticity algorithm. MSC/NASTRAN is used in the development and analysis of structural models, the prediction of linear aeroelastic response of selected wing/store configurations, and the search for configurations speculated herein to produce LCO. The CAPTSDv algorithm is used to carry out relatively fast aeroelastic analyses for inviscid flow and viscous flow through interactive boundary layer coupling, starting with cases previously identified by MSC/NASTRAN as LCO-susceptible. ENS3DAE is then applied to validate CAPTSDv predictions for static aeroelastic and dynamic rigid behaviour for a representative set of flow conditions.

Problem Formulation

The wing studied herein is derived from the "heavy" version of the original Goland wing. Like the original, the heavy wing is structurally represented by a beam, but with additional non-structural mass, as defined by Eastep and Olsen (1980). This latest version, referred to as the Goland[+] wing, is a heavy wing modeled with a box structure to enable a variety of store attachment options.

Geometry

The Goland[+] wing is rectangular and cantilevered from an infinite midplane. A planform schematic is given in Figure 1a (including store) and geometric parameters are assigned values in Table 1. The airfoil section is assumed to be constant over the spanwise extent of the wing and is chosen to be that of a symmetric, parabolic-arc airfoil, defined by $z = 2 \tau_w x (1 - x/c_w)$ $(0 \leq x \leq c_w)$. The wing-tip store is

mounted flush to the wing tip (see Figure 1a). The sectional shape of the store is also assumed to be described by a parabolic arc uniform in the spanwise direction. The leading edge of the store is offset (defined positive) upstream of the wing leading edge, thereby providing the shape formula:

$$z = 2\ \tau_s\ (x + c_{off})\ [1 - (x + c_{off})/c_s] \qquad (-c_{off} \le x \le c_s - c_{off}).$$

Wing Structure and Inertial Properties

The wingbox structure finite element model is built-up from shear panels, modelling the spars and ribs, and membrane elements, modelling the wing skins. In addition, rod elements are included to model spar and rib caps as well as posts that connect the wing skins at every spar/rib intersection. Every element is modelled using the same material properties (shown in Table 1). Notice that the density of this "material" is extremely low. The model was built this way to allow the stiffness and mass properties to be decoupled. This decoupling allows the elements to be sized to tune the model to match the structural dynamic characteristics of the beam model of the heavy Goland wing.

Parameter	Value
c_w, l_w	6, 20
c_s, l_s	10, 1
c_{off}	3
ea	2
τ_w, τ_s	0.04, 0.036
Young's Modulus	1.4976×10^9 slugs/ft^2
Shear Modulus	5.616×10^8 slugs/ft^2
Structural Density	0.0001 slugs/ft^3

Table 1: Selected values of geometric and material parameters.

The geometry of the wing is simple. The origin is at the mid-height of the root of the leading edge spar. The three spars are un-swept and placed at 0, 2 and 4 ft along the positive x-coordinate. The eleven ribs are evenly spaced on 2 ft centres along the positive y-coordinate. The shear elements are defined by the intersections of the spars and ribs, with 10 elements per spar and 2 elements per rib. Next, each spar and rib is 0.33334 ft high and each cell defined by the spars and ribs is capped with a single wing skin membrane element. This results in a total of 40 skin elements. Finally, rods are added on the top and bottom of each shear element and at every spar/rib intersection. The total number of rod elements is 137, consisting of 60 spar caps, 44 rib caps and 33 posts.

The mass properties of this wing are modelled by placing lumped masses with no rotational inertia at each grid point. The lumped masses are sized to match the mass properties (total mass, cg, and inertia) of the heavy Goland wing. For the beam model Goland wing, the mass properties are simply modelled as lumped mass with rotational inertia centred at the cg of sections placed at 2 ft intervals. For the internal rib locations of the (i.e., 2 ft, 4 ft, 6 ft, etc.) beam model, the lumped mass properties were a mass of 22.496 slugs, with a rotational inertia in pitch of 50.3396 slug-ft^2, centred at $x = 2.6$ ft. For the external rib locations (i.e., 0 ft and 20 ft), the lumped mass properties were halved. In the built-up wing model, the masses used for the internal rib locations are as follows: 1.9650 slugs at each leading edge point, 3.9442 slugs at each point on the centre spar; and 5.3398 slugs for the trailing edge points. Also, similar to the beam model, the masses used at the external spar locations are half of the amount used at the internal locations.

The final step in developing the built-up model is sizing the elements so that its structural dynamic characteristics match those of the beam model Goland wing. For this model development, the elements are sized to minimize the error between the first three frequencies of the built-up and beam models. The boundary condition for each model is cantilevered. To maintain symmetry, the elements are grouped by their component. The thicknesses (in ft) for the 2-D elements are: upper and lower wing skins – 0.0155; leading and trailing edge spar – 0.0006; centre spar – 0.0889, and rib – 0.0347. For the 1-D elements, the areas (in ft^2) are: posts – 0.0008; leading and trailing edge spar caps – 0.0416; centre spar cap – 0.1496, and rib cap – 0.0422.

Store Mass and Linkage

The store configuration examined in this work is that of a tip store. This store structure is modelled as a series of rigid bar elements that result in a 10 ft long rigid bar. The resultant bar is centred 0.5 ft outboard of the wing tip and 2 ft aft of the wing leading edge. The store is then rigidly connected to the six wing tip grid points. This is accomplished by defining a seventh wing tip grid point at the centre of the rib structural model (i.e., $x = 2$ ft, $y = 20$ ft, $z = 0$ ft) and connecting this point to the other six points with a MSC/NASTRAN RBE3 element. This results in the displacement of the seventh grid point being the average of the displacements of the original six points. Finally, an RBAR element is used to connect the seventh wing tip point to the corresponding point (i.e., $x = 2$ ft, $y = 20.5$ ft, $z = 0$ ft) of the tip store model.

The mass properties of the tip store are chosen to match the properties of one section of the wing: a mass of 22.496 slugs and a rotational inertial of 50.3396 slug-ft^2. During this study, the position of the store mass is fixed at the lateral and vertical centres of the store (i.e., $y = 20.5$ ft and $z = 0$ ft) and varied in the streamwise direction.

Computational Aeroelasticity Methods

CAPTSD and CAPTSDv

CAPTSD solves the three-dimensional, transonic, small-disturbance, potential-flow equations for partial and complete aircraft configurations (Batina (1988,1989)). The standard, most widely distributed version of the program computes inviscid, compressible flow for combinations of wings, fuselage, horizontal tail, bodies/stores, and rectangular planform vertical surfaces. CAPTSD solves the aerodynamic equations of motion using a time-accurate algorithm that is capable of simulating both steady and unsteady flow (Batina (1992)). The method is capable of computing aeroelastic interactions by coupling the aerodynamic module with a structural dynamics simulation. The structural dynamics of horizontal surfaces are simulated in CAPTSD by using a modal structural model. The structural analysis is coupled to the aerodynamic analysis by a process that transfers generalized aerodynamic forces and generalized displacements between the aerodynamics and structural dynamics modules. Using this approach, CAPTSD is capable of simulating both static and dynamic aeroelastic phenomena.

A viscous-inviscid interaction version of CAPTSD, known as CAPTSDv, has been developed (Howlett (1987), Edwards (1993)) and applied to a variety of problems involving mildly separated and separation onset flows (Edwards (1998)). The method couples the inviscid CAPTSD algorithm with an inverse integral boundary layer model. The boundary layer equations are solved in a quasi-steady formulation similar to that recommended by Green et al. (1977). The outer inviscid solution and the inner viscous solution are computed independently and are coupled using an active control mechanism that minimizes coupling errors for unsteady flows. In this investigation, a single version of the CAPTSDv algorithm is used to perform both inviscid and viscous aeroelastic analysis (execution mode controlled by user).

CAPTSD solves the equations of motion on a sheared Cartesian grid system where lifting surfaces are modeled as thin plates. Thickness and camber information for the upper and lower surfaces of each lifting surface is supplied through a set of surface slopes that are specified as boundary conditions for the algorithm. Similarly, structural mode shapes are supplied as surface slope perturbations. This approach greatly simplifies the modelling task required for an aeroelastic analysis, since the grids are typically simple to generate, and no moving grid algorithm is required for the aeroelastic simulation. CAPTSD is

1-1.5 orders of magnitude more computationally efficient than higher fidelity methods, and offers the potential for nonlinear aerodynamics analysis within a design framework using the CAPTSD methodology.

ENS3DAE

Aeroelastic analysis of the Euler and Navier-Stokes equations is carried out with the Euler/Navier-Stokes 3-Dimensional Aeroelastic (ENS3DAE) method. The Lockheed-Georgia Company, under contract to the Air Force Wright Laboratory, developed ENS3DAE in the late 1980's (Schuster *et al.* (1990)). This program has been used to solve numerous aerodynamic and aeroelastic problems about a wide range of geometries including wings, wing/fuselage, wing/control system, propulsion, and integrated airframe/propulsion configurations (Smith *et al.* (1996), Schuster *et al.* (1998), Lewis and Smith (2000)).

ENS3DAE solves the full three-dimensional compressible Reynolds averaged Navier-Stokes equations, the thin layer approximation to these equations, or the Euler equations using an implicit approximate factorization algorithm. Central finite differences are used for spatial discretization, and a three-dimensional implementation of the Beam-Warming implicit scheme is employed for the temporal integration. Blended second- and fourth-order dissipation is added to the explicit right-hand-side of the equations, and implicit second-order dissipation is added to improve the diagonal dominance of the matrix system. For time-accurate cases, global or local time stepping within an inner sub-iteration loop for each physical time step is employed. The sub-iteration procedure effectively removes the stability limit on the time-step for unsteady flow cases, and improves the temporal accuracy of the method, provided that relevant time-scales within the computed flow field are captured by the selected time step and that a sufficient number of sub-iterates are computed.

The method accepts either single- or multiple-block curvilinear grids. Boundary conditions are imposed explicitly on each computational face of each grid block and the current release of the program requires a one-to-one match of grid points at block interfaces. Turbulence characteristics are predicted using the Baldwin-Lomax algebraic turbulence model or the Johnson-King model (Huttsell *et al.* (2001)). The code is written to take advantage of vectorization; directives for parallel operation on shared memory processors are also included in the programming. The method is regularly executed on eight or more processors.

A linear generalized mode shape structural model is closely coupled with the aerodynamic method to analyse structurally flexible vehicles. ENS3DAE uses a highly efficient, grid-motion algorithm for aeroelastic and control-surface simulations that is based on an algebraic shearing technique. Since dynamic aeroelastic and oscillating control surface simulations require grid models that deform in time, the algorithm now enforces the Geometric Conservation Law (Thomas and Lombard (1979)).

Results

Physical Conditions

The aeroelastic analysis is carried out with enforced consistency between velocity and dynamic pressure, assuming constant density at sea-level conditions. Mach number and Reynolds number are treated as independent variables, such that match-pointed conditions are not achieved. Reynolds number is not varied in this investigation. Structural damping is assumed to vanish for all baseline cases investigated. The selected values of various parameters are summarized in Table 2.

Summary of Grid Construction

Three grids are constructed for the CAPTSDv calculations reported in this paper. Owing to the geometry of the wing/store configuration and the mid-plane formulation of the surface boundary condition used in CAPTSDv, these grids are rectilinear. Clustering of grid points is enforced along the edges of the geometry and normal to the wing and store surfaces. Grids are generated by first computing grid-point distributions in each of the three coordinate directions external to CAPTSDv, subject to the specified clustering conditions, and then using the generator internal to CAPTSDv to obtain the full rectilinear

grid. The first grid (G1) is used for inviscid, clean-wing and wing/store (store mass only) computations; the second grid (G2) is used for inviscid, wing/store computations, and the third grid (G3) is used for viscous clean-wing and wing/store (store mass only) computations. The values of parameters governing grid construction are given in Table 3.

Parameter	Value
ρ_∞	0.0023771
T_∞	518.67
Re_∞	15×10^6
α_o	0
ζ	0

Table 2: Selected values of physical parameters.

Parameter	Grid G1	Grid G2	Grid G3
Domain Size (x,y,z)	(41,13.5,40)	(41,13.5,40)	(41,13.5,40)
Grid Dimensions (i,j,k)	(90,55,60)	(90,55,60)	(150,55,60)
Leading-Edge Spacing	0.01	0.01	0.008
Trailing-Edge Spacing	0.01	0.01	0.008
Normal Spacing (top, bottom)	(0.002,0.002)	(0.002,0.002)	(0.002,0.002)
Wing-Tip Spacing	0.025	0.025	0.025
Wing Index Dimensions (i,j)	(41,32)	(41,32)	(101,32)
Store Index Dimensions (i,j)	N/A	(57,5)	N/A

Table 3: Selected values of CAPTSDv grid parameters (lengths in wing chords, c_w).

A view of grid G2 in the x-y plane in the neighborhood of the wing/store configuration is shown in Figure 2a to illustrate the effect of grid clustering along the combined planform.

For the ENS3DAE calculations presented in this paper, only the clean wing (to which the store mass may be added) is considered. A two-block, HH-type grid is used for this configuration and is generated with GRIDGEN V13. The two blocks have equal dimensions and grid spacings, and correspond to the upper and lower halves of the computational space. It should be noted that the wing-tip geometry is slightly modified from the description given above to close the tip and simplify the grid-generation process. Characteristics of the grid are given in Table 4.

Contrary to the convention shown in Figure 1a, in ENS3DAE, the physical coordinates are defined with x streamwise, y normal, and z spanwise. However, consistent with CAPTSDv, the computational coordinates are defined with i streamwise, j spanwise, and k normal. Figure 2b shows a portion of the grid in the root plane. The inset shows a highly magnified view of the leading edge and highlights a gap between the upper and lower blocks equal to 0.053% of the chord. A sharp leading edge is difficult to model using an Euler/Navier-Stokes solver; the gap helps by removing the leading edge from the computational domain. The leading edge is captured numerically through the boundary conditions applied at points around the physical leading edge. In the spanwise direction, the wing tip is modeled by

transitioning the geometry from the full airfoil thickness at the wing tip to zero thickness at the first spanwise station outboard of the wing tip.

Parameter	Value
Domain Size (x,y,z)	(406,400,80)
Block Dimensions (i,j,k)	(161,71,51)
Leading-Edge Spacing	0.02
Trailing-Edge Spacing	0.02
Normal Spacing	0.0006667
Wing-Tip Spacing	0.05
Wing Index Dimensions	(81,41)

Table 4: Selected values of ENS3DAE grid parameters (lengths in feet).

Modal Analysis

Modes of the structural model are computed with MSC/NASTRAN and then splined to aerodynamic surface grids (specified at $z = 0$) with the infinite plate spline, as implemented by Smith *et al.* (1995, 1996). The modes are scaled to yield generalized masses of magnitude 1. Modal amplitudes are computed through time integration of the generalized structural dynamics equations to yield updated approximations of wing/store surface deflections. Unless otherwise stated, results given in this paper are obtained by retaining the 4 modes of lowest frequency in the aeroelastic analysis and by excluding in-plane modes. Sets of retained of modes are shown in Figure 3 for two cases: clean wing with no store and wing with store mass positioned 1.75 feet forward of the wing elastic axis (see discussion below). With the exception of mode 4, the modes in the two sets are quite similar; slightly more torsion is evident at the wing tip in the modes associated with the clean wing.

Linear Analysis

To determine a parameter space (velocity and Mach number for specified altitude) where store-induced LCO possibly exists, a linear flutter analysis of a clear wing and a wing/tip store combination is conducted. The linear flutter speeds (those from linear aerodynamic theories) are determined from data calculated from the *p-k* method of MSC/NASTRAN. The flutter and divergence instabilities can be determined from an inspection of calculated data in graphical form, the so-called *V-g* and *V-ω* diagrams. These diagrams are shown in Figures 4a (clean wing) and 4b (wing with tip store mass) for a selected Mach number of 0.92. From Figure 4a, the flutter speed of a clean wing is determined by the first crossing of one of the modes from negative to positive values of the damping parameter, *g* (i.e., 334 ft/sec), and a corresponding flutter frequency of 2.17 HZ. Additionally, shown in Figures 4a is a divergence instability, whose speed is determined by the simultaneous occurrence of zero damping and zero frequency for another mode (i.e., 630 ft/sec).

The *V-g* diagram of the clean wing is compared to the *V-g* diagram of the wing/store configuration (mass only), shown in Figure 4b, when the store *cg* is located 1.75 ft upstream of the wing *ea* (equivalent to the store pitch axis). By comparing the two diagrams, it is seen that the flutter speed is increased to 559 ft/sec when the store *cg* is placed at this position and that the severity of the flutter instability of the clean wing has been reduced (reflected by less damping). The flutter mode of the wing/store has been converted into a "hump," or lightly damped mode. It is speculated that the initiation of store-induced LCO is associated, in some way, with hump modes, such that the linear flutter investigation defined a beginning region to search for LCO. Of course, since this hump is determined from linear aerodynamics, the region of LCO must be modified by taking into consideration transonic (nonlinear) aerodynamics. This modification is discussed in the following sections for a determination of store-induced LCO.

Linear analysis is carried out for other store mass positions, but not reported herein. These results show the reduction of the peak damping parameter with forward movement of the store mass. The offset position of 1.75 ft (upstream of the wing *ea*) is selected for use in the CAPTSDv calculations reported below, because of the small peak value of *g* attained with this parameter value.

Flutter Boundaries

Boundaries of flutter and LCO onset are computed for the clean wing configuration and for the wing with store mass (i.e., store not modeled aerodynamically). The flow is assumed to be inviscid. These results are compared to those obtained with MSC/NASTRAN using linear analysis. LCO solutions are observed at Mach numbers above Mach 0.9 when the store mass is present; these cases will be discussed in greater detail in the next section. Flutter and LCO boundaries are compared in Figure 5a. For the clean wing, CAPTSDv predicts a flutter speed of 433 ft/sec at Mach 0.7, a value 3.5% higher than that predicted by MSC/NASTRAN. With the store mass included, CAPTSDv predicts a flutter speed of 648.5 ft/sec (CAPTSDv), a value 6.8% higher than that provided by MSC/NASTRAN. At Mach 0.7, the aerodynamics are linear and the reasonable comparisons between CAPTSDv and MSC/NASTRAN are to be expected. CAPTSDv clearly confirms that forward movement of the store mass has a stabilizing effect on the aeroelastic system for Mach numbers at or below 0.9.

As Mach number increases beyond 0.7, the clean-wing flutter boundary obtained with CAPTSDv develops a transonic dip with a minimum flutter speed (355 ft/sec) at about Mach 0.88. The boundary is much flatter when the store mass is included; flutter speed averages around 645 ft/sec. Both boundaries show a rapid increase in flutter speed near Mach 0.9. However, at selected Mach numbers between 0.90 and 0.95 (0.91, 0.92, 0.93, and 0.94) with the store mass present, LCO solutions are observed. These nonlinear oscillations are computed at flight speeds much lower than the nominal, wing/store flutter speed, and, for some Mach numbers, lower than the clean-wing flutter speed. Thus, the presence of the store destabilizes the system at higher Mach numbers in an adverse manner, i.e., to lower flight speeds.

On the flutter boundary for the wing/store configuration, two different flutter modes are observed. These are contrasted in terms of the computed lift and moment coefficients (taken about the leading edge) for Mach 0.84 and Mach 0.9, as shown in Figures 5b and 5c. Note that unstable test points are selected above the flutter boundary: $U = 750$ ft/sec at Mach 0.84 (flutter at 642.5 ft/sec) and U = 850 ft/sec at Mach 0.9 (flutter at about 825 ft/sec). Two different frequencies of divergent oscillation are observed: 1.90 Hz (Mach 0.84) and 9.52 Hz (Mach 0.90). These frequencies are somewhat larger than the natural frequencies corresponding to modes 1 (1.69 Hz) and 3 (9.17 Hz), respectively. For both flutter modes, the phase relationships between peak lift and moment are the same (about 180 degrees out of phase). Differences in frequency correlate well with differences in modal participation between the flutter modes. As shown in Figures 5d and 5e, response is dominated by modes 1 and 2 at Mach 0.84, whereas modes 3 and 4 dominate the response at Mach 0.9. The impact of varying modal participation on wing shape is described in the next section.

A switching of flutter modes is perhaps suggested by the linear MSC/NASTRAN results shown for Mach 0.92 in Figure 4 (the results for Mach 0.9 are not markedly different). The effect of nonlinearity appears to be large in terms of stabilizing the interaction between modes 1 and 2, predicted by MSC/NASTRAN to occur at about 560 ft/sec. At a larger frequency, coalescence of modes 3 and 4 is evident in the MSC/NASTRAN results at a flight speed of about 800 ft/sec, a velocity near the flutter speed predicted by CAPTSDv.

Store-Induced Limit-Cycle Oscillation

In a Mach number range between 0.91 and 0.95, fully developed LCO states are computed with CAPTSDv for the wing/store configuration, excluding store aerodynamics (see Figure 5a). As will be shown later, the effect of including store aerodynamics is not significant, while the effect of viscosity is to reduce LCO amplitude. Two types of LCO are observed: (1) an expected form involving significant time-periodic oscillations of the aeroelastic system that will be described first and referred to as simply LCO, and (2) an unexpected form with very small amplitudes (~3 orders of magnitude less in magnitude) that will be described second and referred to as "embryonic" LCO, or ELCO.

As shown in Figure 5a, LCO is observed over a restricted range of Mach numbers. Generally, LCO amplitudes increase with increasing velocity, and for sufficiently large velocities, computed oscillations become so large that the assumptions of TSDT become invalid. Attention is first given to Mach 0.92, where LCO is first observed at $U = 390$ ft/sec for inviscid flow (onset occurring between 385 and 390 ft/sec) and $U = 410$ ft/sec for viscous flow (onset occurring between 390 and 410 ft/sec). It should be noted that the onset of LCO is computationally expensive to obtain, since very large integration times are necessary for the aeroelastic system to approach time-asymptotic behavior at values of flight speed near critical. In these calculations, the initial state is defined by a flow solution given by a rigid-body calculation, and the modal amplitudes are assumed to vanish, except for the first mode, which is assigned an initial value of 0.01.

The slow growth of lift coefficient to its asymptotic value is shown in Figure 6a for $U = 410$ ft/sec, assuming inviscid flow. LCO frequency is observed to be 2.92 Hz. Time histories of fully developed lift and moment coefficient are shown in Figure 6b; the phase relationship between these quantities is similar to that observed for the two flutter modes previously described. The computed frequency corresponds to the modal content of the aeroelastic response. As seen in Figure 6c, mode 2 (a natural frequency of 3.05 Hz) dominates the response, with strong participation also from mode 1. At this Mach number and flight speed, the first two modes are much more strongly coupled than in the flutter mode found at low transonic Mach numbers (cf. Mach 0.84), with an associated increase in response frequency.

A similar set of plots of LCO response are shown in Figure 7 for the case of viscous flow, assuming an equivalent flight speed of 410 ft/sec at Mach 0.92. Grid G3 is used for viscous calculations, and the aerodynamics of the store are assumed negligible. LCO amplitude is observed to diminish through the effects of viscosity, and frequency slightly increases to 2.99 Hz. Viscous simulations of LCO are somewhat stiffer than inviscid computations, requiring one Newton sub-iterate per time step for stable calculation.

Structural response associated with LCO is contrasted with that of the two flutter modes through visualization of wing-tip motion. Snapshots of instantaneous chordline orientation (lines connecting wing tip leading edge and trailing edge) are shown in Figure 8 for each of the three characteristic aeroelastic responses. The low-speed flutter mode is primarily first bending, which is reflected by a vertical displacement of the wing tip at different times, with introduction of only a slight incidence angle with respect to the freestream. The flutter mode observed at Mach 0.9 is a higher frequency mode involving significant contributions from modes 3 and 4. The response of the wing tip involves both pitch and plunge, with a motion akin to that of a ship moving into ocean waves (a visual rotation about the mid-chord). In the situation of LCO, the response is composed of first bending and first torsion contributions. A pitching motion dominates the resulting movement of the wing tip, with visual rotation about the tip leading edge.

LCO solutions of the type described above are not observed at flight speeds below 390 ft/sec for inviscid flow at Mach 0.92. However, at speeds between 340 and 390 ft/sec, sustained oscillations of very small amplitude and less regular character are computed. In this speed range, the magnitude of system oscillations increases very slowly with increasing U. These ELCO states appear to be physical and not numerical in origin, since ELCO formation is found to be persistent to variation of Mach number and various numerical parameters. However, ELCO amplitude is sensitive to structural damping and the numerical precision of the computation. When ζ is increased from the baseline value of 0 to 0.03, ELCO amplitude is reduced by over a factor of 5 at $U = 385$ ft/sec, and is found to vanish at $U = 350$ ft/sec. Also, increasing the baseline precision of the computation to double, ELCO amplitude is observed to grow considerably (but remaining at levels small compared to LCO).

A time history of lift coefficient is shown in Figure 9 for $U = 385$ ft/sec and assuming baseline values of numerical parameters: the frequency of 2.94 Hz is nearly identical to that found during LCO at $U = 410$ ft/sec, while peak lift coefficient reaches only about 5×10^{-5}.

LCO Sensitivities

The variation of LCO amplitude with respect to changes in flight speed at Mach 0.92 is computed for three categories of analysis: inviscid analysis of wing with store mass (grid G1); inviscid analysis of wing

with store modeled aerodynamically (grid G2), and viscous analysis of wing with store mass (grid G3). Results are compared in Figure 10a to show the effects of varying the level of modeling fidelity within the context of transonic small-disturbance theory. Assuming inviscid flow, it is observed that modelling the store aerodynamically has little impact on the onset or computed amplitude of LCO. However, at speeds exceeding 420 ft/sec, solutions can not be stably computed. In these cases of increased wing-tip twist, numerical destabilization appears to be a result of a very large, localized, pressure spike observed in the region of the juncture between the store and the wing leading edge. This destabilization occurs at about the speed for which LCO amplitude is predicted to grow rapidly when store aerodynamics are ignored; peak lift coefficient begins to take a large jump at $U = 427$ ft/sec with this approximation. At speeds exceeding this value, the validity of the computed inviscid solutions is considered to be diminished, owing to the small-disturbance nature of the methodology. As described above for $U = 410$ ft/sec, the effect of viscosity is to diminish LCO amplitude. When the boundary layer thickness is modelled, no large increase in LCO amplitude is observed, and peak lift coefficient remains bounded by 0.26 over the range of speeds examined, thus reducing the deformation of the wing and extending the speed range over which the assumption of small disturbances is arguably satisfied. Near the bifurcation point, at $U = 388$ ft/sec, non-unique states are observed. One state, obtained with the baseline initial conditions exhibits very small-amplitude ELCO behavior, while the other state, obtained by restarting the aeroelastic solution from $U = 390$ ft/sec, exhibits LCO behavior. However, as velocity is reduced below 388 ft/sec, only ELCO is observed, and as velocity is increased above this same speed, only LCO is observed. These results are indicative of the presence of a subcritical bifurcation just above this speed, causing relatively large jumps in LCO amplitude over a small range of flight speeds. This phenomenon is explored further below for Mach 0.93.

The variation of peak lift coefficient with velocity is found to be more regular at Mach 0.93 than at Mach 0.92. For this higher Mach number, the effects of variation of root angle-of-attack are assessed in Figure 10b using the observed half-differentials between maximum and minimum lift coefficient (to separate the dependence of oscillation amplitude on velocity from the dependence of static aeroelastic response on velocity). When α_0 is increased to 2 degrees, a considerable decrease in LCO amplitude is observed, along with a significant delay in LCO onset to higher velocities.

As stated above for the results computed at Mach 0.92 (cf. Figure 10a), the onset of LCO is subcritical. This is also observed at Mach 0.93, as shown in detail in Figure 11 (for the baseline condition of vanishing root angle-of-attack). For this comparison, aeroelastic solutions are computed using two kinds of initial conditions: the initial conditions described above, and initialisation of the flowfield using a fully developed LCO solution obtained at a higher velocity. It is seen that the latter class of initial condition produces fully developed LCO solutions for a small range of velocities (noted at 386 ft/sec and 388 ft/sec) at which the former class of initial condition does not produce LCO. While the range of hysteresis is slight, the subcritical nature of the bifurcation does explain the rather large jumps in amplitude observed beyond the critical points.

Not surprisingly, over the range of Mach numbers that sustain LCO, amplitude of response is found to be highest over the midsection of the range. This is shown in Figure 12 for a velocity of 410 ft/sec. The response near the low-Mach boundary of the LCO region is characteristic of the subcritical response shown in Figures 10a and 11. However, at the high-Mach boundary of the LCO region, the computed results are not suggestive of non-unique flow responses.

Comparisons with ENS3DAE

To assist in the validation of the transonic aeroelastic modeling employed in CAPTSDv, CAPTSDv solutions (inviscid) are compared to ENS3DAE (Euler) solutions for two clean-wing calculations: prediction of static aeroelastic response for a root angle-of-attack of 2 degrees and dynamic response of a rigid wing undergoing 3-Hz pitch oscillations of ½ degree in amplitude. Both cases show good agreement between the Euler and TSDT results, and are reported here for a transonic condition ($U = 400$ ft/sec and Mach 0.92) in terms of the predicted values of lift and moment coefficients. For the case of static aeroelastic response, C_L predictions agree within 6% (0.126 for ENS3DAE and 0.134 for CAPTSDv) and C_M predictions agree within 15% (-0.0687 for ENS3DAE and –0.0809 for CAPTSDv). In the case of

response to forced pitch oscillations, lift and moment coefficients are compared in Figure 13 as phase portraits, where it is seen that amplitudes and phase relationships are in excellent agreement.

Summary and Conclusions

A class of limit-cycle oscillations was observed for a rectangular wing with tip store. These LCOs occurred at speeds lower than that predicted using linear aerodynamics and at speeds lower than that computed for the clean-wing configuration. The form of the bifurcation was subcritical, such that LCO amplitude jumped abruptly as Mach number increased beyond a critical value. However, it was also found that as Mach number increased to a critical value (~0.94–0.95), LCO states could no longer be sustained. For the configurations examined, the presence of LCO was insensitive to the inclusion of store aerodynamics in the aeroelastic model. Also, the effect of viscosity was to diminish LCO amplitude. A second class of LCO solutions with small amplitude was observed that occurred over a range of speeds below critical, i.e., prior to the initiation of LCOs characterized by large-amplitude aeroelastic response. These states were found to be sensitive to structural damping, such that addition of nominal levels of damping was sufficient to overcome the phenomenon.

The search for LCO states was conducted in two steps. First, linear theory was employed in the identification of "hump" modes, which corresponded to placement of the store mass near the wing leading edge. Such characteristic aeroelastic responses were expected to point to conditions susceptible to LCO. Second, LCO states were computed using the transonic small-disturbance theory algorithm CAPTSDv, assuming both inviscid and viscous flow. This nonlinear mathematical formulation was sufficient to capture properly weak shock formation and movement. The validation of these LCO results using higher fidelity methods (i.e., Euler and Navier-Stokes via ENS3DAE) is currently underway, and preliminary results are encouraging. Also, static aeroelastic and dynamic rigid responses of the clean wing computed with CAPTSDv and ENS3DAE are in close agreement. Additional work is planned for the study of LCO including the presence of underwing stores and for the study of a swept-wing configuration. Further investigation is required to yield a full explanation of LCO development for the wing/store configuration examined herein and to better understand any potential connection between the observed nonlinear LCO phenomenon and the development of hump modes in the reported linear analysis.

Acknowledgements

References

1. Batina, J. T., "Efficient Algorithm for Solution of the Unsteady Transonic Small-Disturbance Equation," *Journal of Aircraft*, Volume 25, July 1988, pp. 598-605.
2. Batina, J. T., "Unsteady Transonic Algorithm Improvements for Realistic Aircraft Applications," *Journal of Aircraft*, Volume 26, February 1989, pp. 131-139.
3. Batina, J. T., "A Finite Difference Approximate-Factorization Algorithm for Solution of the Unsteady Transonic Small-Disturbance Equation," NASA TP 3129, January 1992.
4. Denegri, C. M., "Limit Cycle Oscillation Flight Test Results of a Fighter with External Stores," Journal of Aircraft, Volume 37, Number 5, September-October 2000, pp. 761-769.
5. Edwards, J. W., "Transonic Shock Oscillations Calculated with a New Interactive Boundary Layer Coupling Method," AIAA Paper 93-0777, January 1993.
6. Eastep, F. E., "Transonic Flutter Analysis of a Rectangular Wing with Conventional Airfoil Sections," AIAA Journal, Volume 18, Number 10, October 1980, pp. 1159-1164.

7. Edwards, J. W., "Calculated Viscous and Scale Effects on Transonic Aeroelasticity," AGARD-R-822, Numerical Unsteady Aerodynamic and Aeroelastic Simulation, March 1998, pp. 1-1 – 1-11.
8. Farhat, C., Pierson, K., and Degand, C., "CFD Based Simulation of the Unsteady Aeroelastic Response of a Maneuvering Vehicle," AIAA Paper 2000-0899, January 2000.
9. Green, J. E., Weeks, D. J., and Brooman, J. W. F., "Prediction of Turbulent Boundary Layers and Wakes in Compressible Flow by a Lag-Entrainment Method," R & M No. 3791, British Aeronautical Research Council, 1977.
10. Howlett, J. T., "Efficient Self-Consistent Viscous Inviscid Solution for Unsteady Transonic Flow," *Journal of Aircraft*, Volume 24, November 1987, pp. 737-744.
11. Huttsell, L., Schuster, D., Volk, J., Giesing, J., and Love, M., "Evaluation of Computational Aeroelasticity Codes for Loads and Flutter," AIAA Paper 2001-0569, January 2001.
12. Lewis, A. P. and Smith, M. J., "Euler-Based Aeroelastic Analysis of Shell Structures," *Journal of Aircraft*, Vol. 37, No. 5, September-October 2000, pp. 840 - 845.
13. Melville, R., "Nonlinear Simulation of F-16 Aeroelastic Instability," AIAA Paper 2001-0570, January 2001.
14. Melville, R., "Nonlinear Mechanisms of Aeroelastic Instability for the F-16," AIAA Paper 2002-0871, January 2002.
15. Schuster, D. M., Beran, P. S., and Huttsell, L. J., "Application of the ENS3DAE Euler/Navier-Stokes Aeroelastic Method," AGARD-R-822, Numerical Unsteady Aerodynamic and Aeroelastic Simulation, March 1998, pp. 3-1 – 3-11.
16. Schuster, D. M., J. Vadyak, and E. Atta, "Static Aeroelastic Analysis of Fighter Aircraft Using a Three-Dimensional Navier-Stokes Algorithm," *Journal of Aircraft*, Volume 27, Number 9, September 1990, pp. 820-825.
17. Smith, M. J., Hodges, D. H., and Cesnik, C. E. S., "An Evaluation of Computational Algorithms to Interface between CFD and CSD Methodologies," WL-TR-96-3055, November 1995.
18. Smith, M. J., Schuster, D. M., Huttsell, L. J., and Buxton, B., "Development of and Euler/Navier-Stokes Aeroelastic Method for Three-Dimensional Vehicles with Multiple Flexible Surfaces," AIAA Paper 96-1400, April 1996.
19. Smith, M. J., Hodges, D. H., and Cesnik, C. E. S., "Evaluation of Computational Algorithms Suitable for Fluid-Structure Interactions," *Journal of Aircraft*, Volume 37, Number 2, March-April 2000, pp. 292-294.
20. Thomas, P. D., and Lombard, C. K., "Geometric Conservation Law and Its Application to Flow Computations on Moving Grids," *AIAA Journal*, Volume 17, Number 10, October 1979, pp. 1030 - 1037.
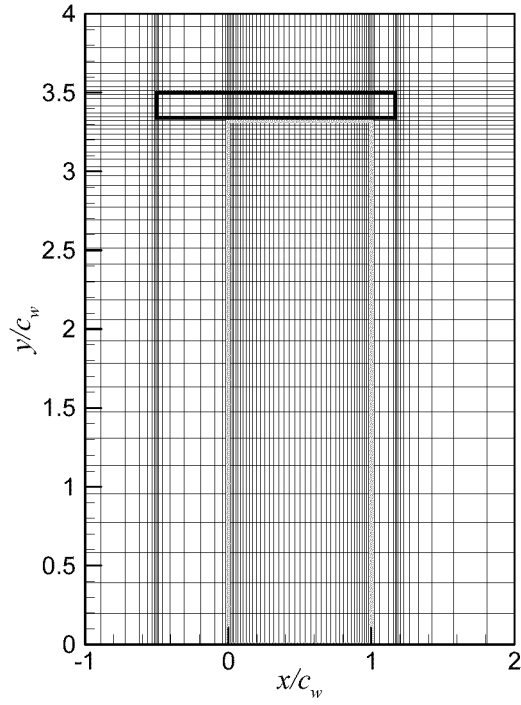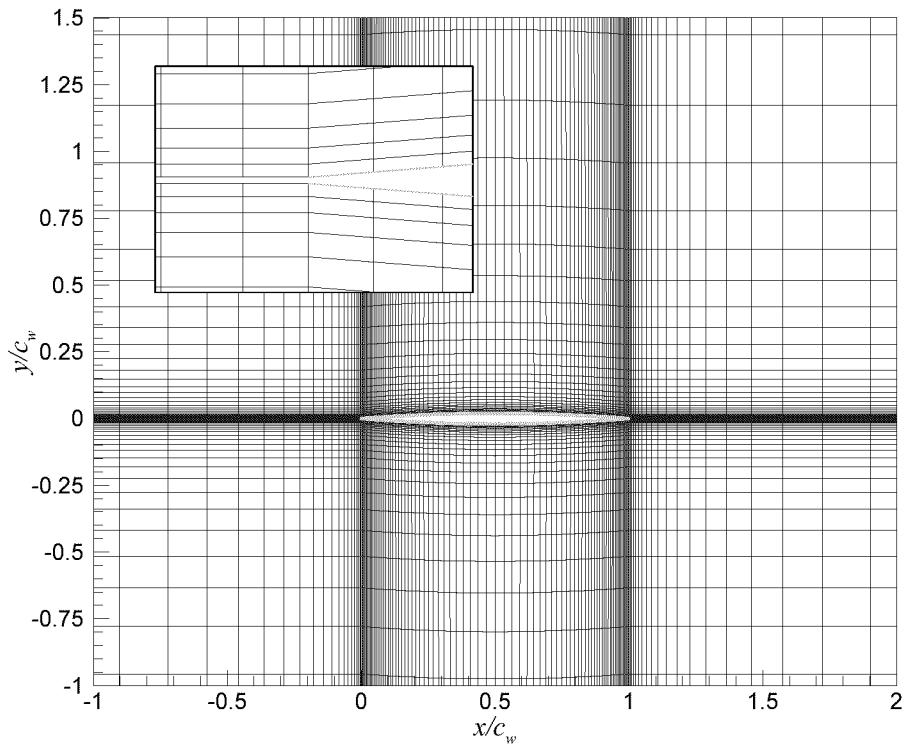
(a) Planform geometry

■ Structural Grid Point

20 ft

4 ft

1/3 ft
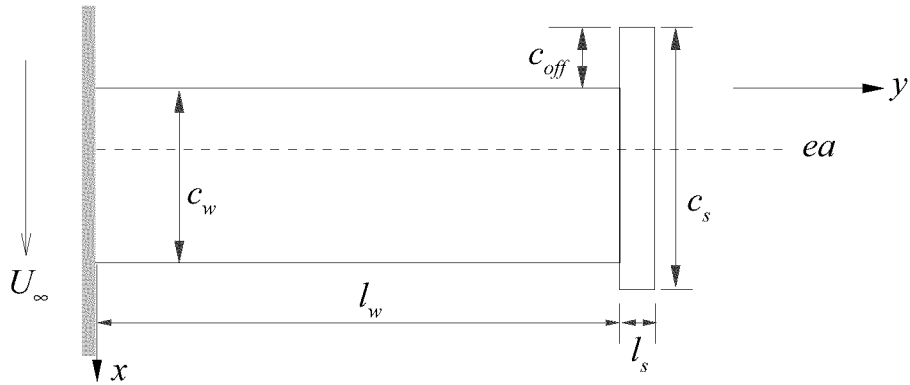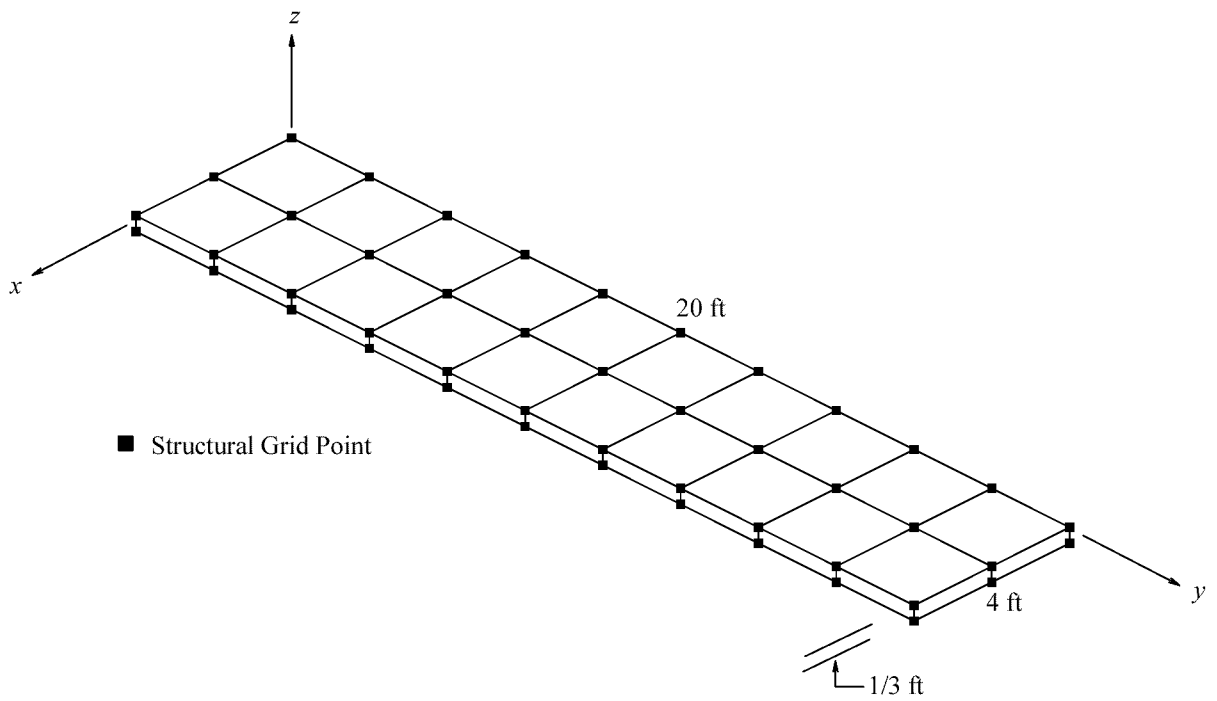
(b) Structural model

Figure 1: Schematics of Goland[+] Wing geometry and structural model.

(a) CAPTSDv wing surface grid (G2): grid lines (red); wing boundary (green); store boundary (blue)

(b) ENS3DAE root-plane grid (inset figure shows leading edge): grid lines (red); wing boundary (green)

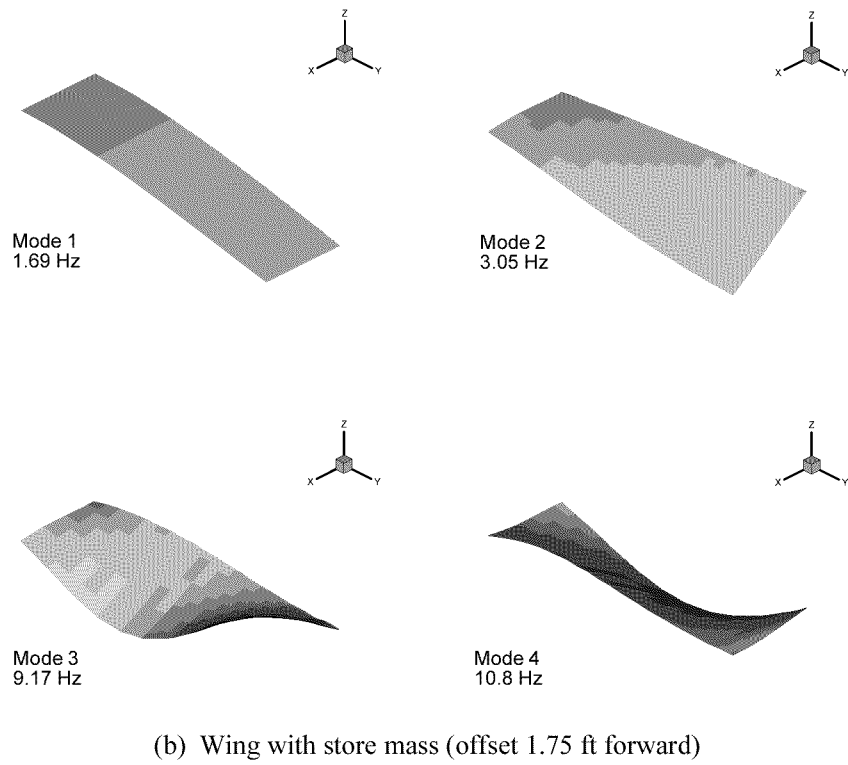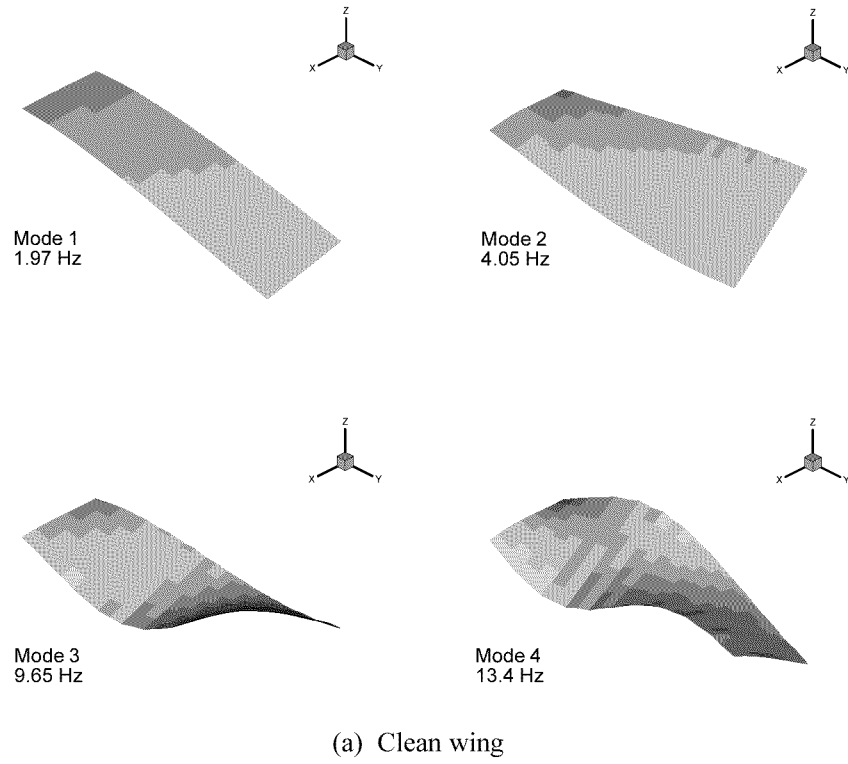**Figure 2**: CAPTSDv and ENS3DAE computational grids for Goland^{+} Wing.

Mode 1
1.97 Hz

Mode 2
4.05 Hz

Mode 3
9.65 Hz

Mode 4
13.4 Hz

(a) Clean wing

Mode 1
1.69 Hz

Mode 2
3.05 Hz

Mode 3
9.17 Hz

Mode 4
10.8 Hz

(b) Wing with store mass (offset 1.75 ft forward)

Figure 3: Splined modes retained in aeroelastic analysis of Goland$^+$ wing with and without store mass.

(a) Clean wing damping and frequencies   (b) Wing/store damping and frequencies

Figure 4: Damping and frequency characteristics predicted by linear aeroelastic analysis (MSC/NASTRAN) for the Goland[+] wing with and without store mass at Mach 0.92.
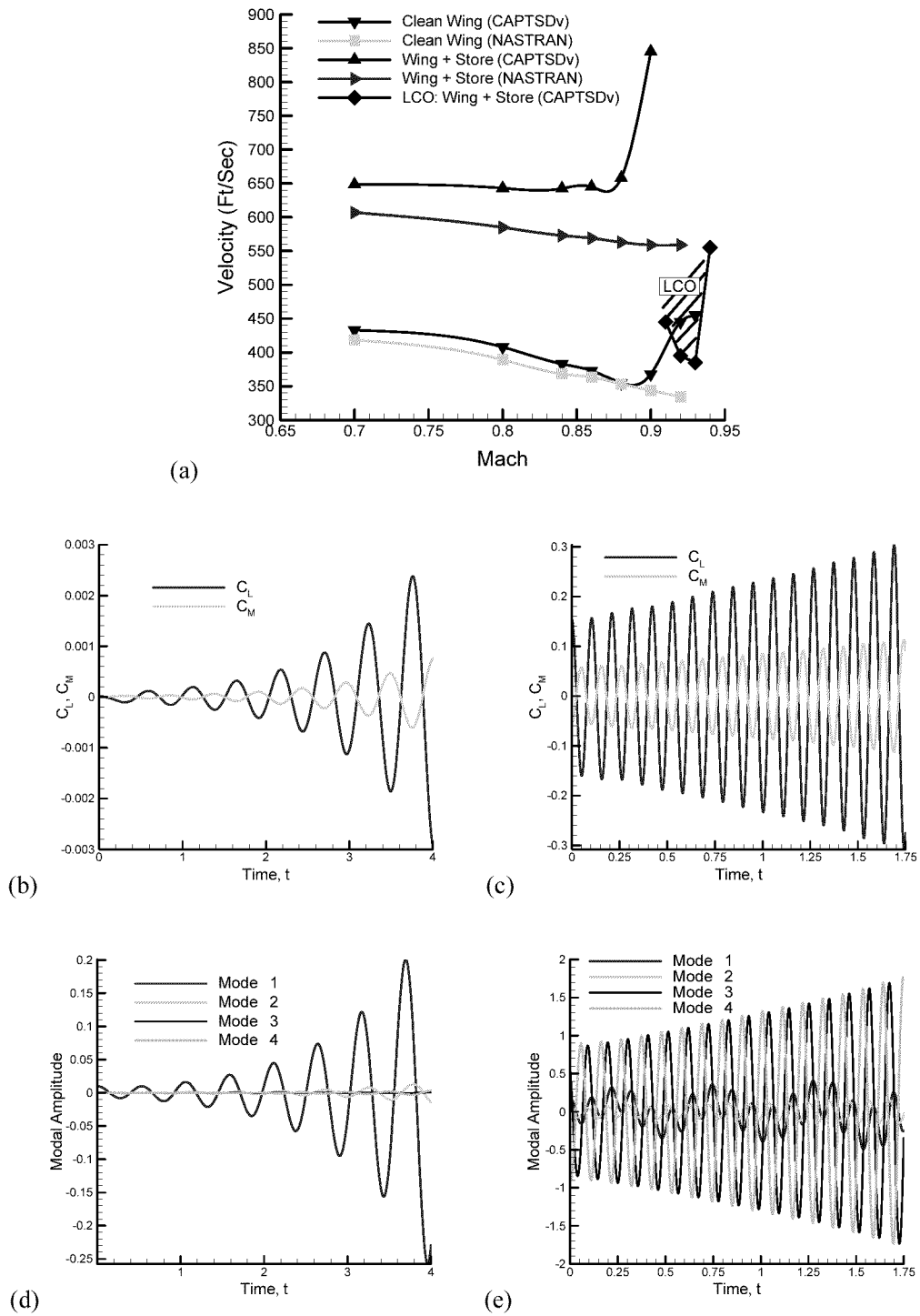
Figure 5: Inviscid CAPTSDv aeroelastic analysis for grid G1 without store aerodynamics: (a) comparison of flutter and LCO boundaries computed with CAPTSDv and MSC/NASTRAN; (b) and (c) force and moment coefficient histories for Mach 0.84 (U = 750 ft/sec) and Mach 0.90 (U = 850 ft/sec); (d) and (e) modal amplitude histories for Mach 0.84 (U = 750 ft/sec) and Mach 0.90 (U = 850 ft/sec).
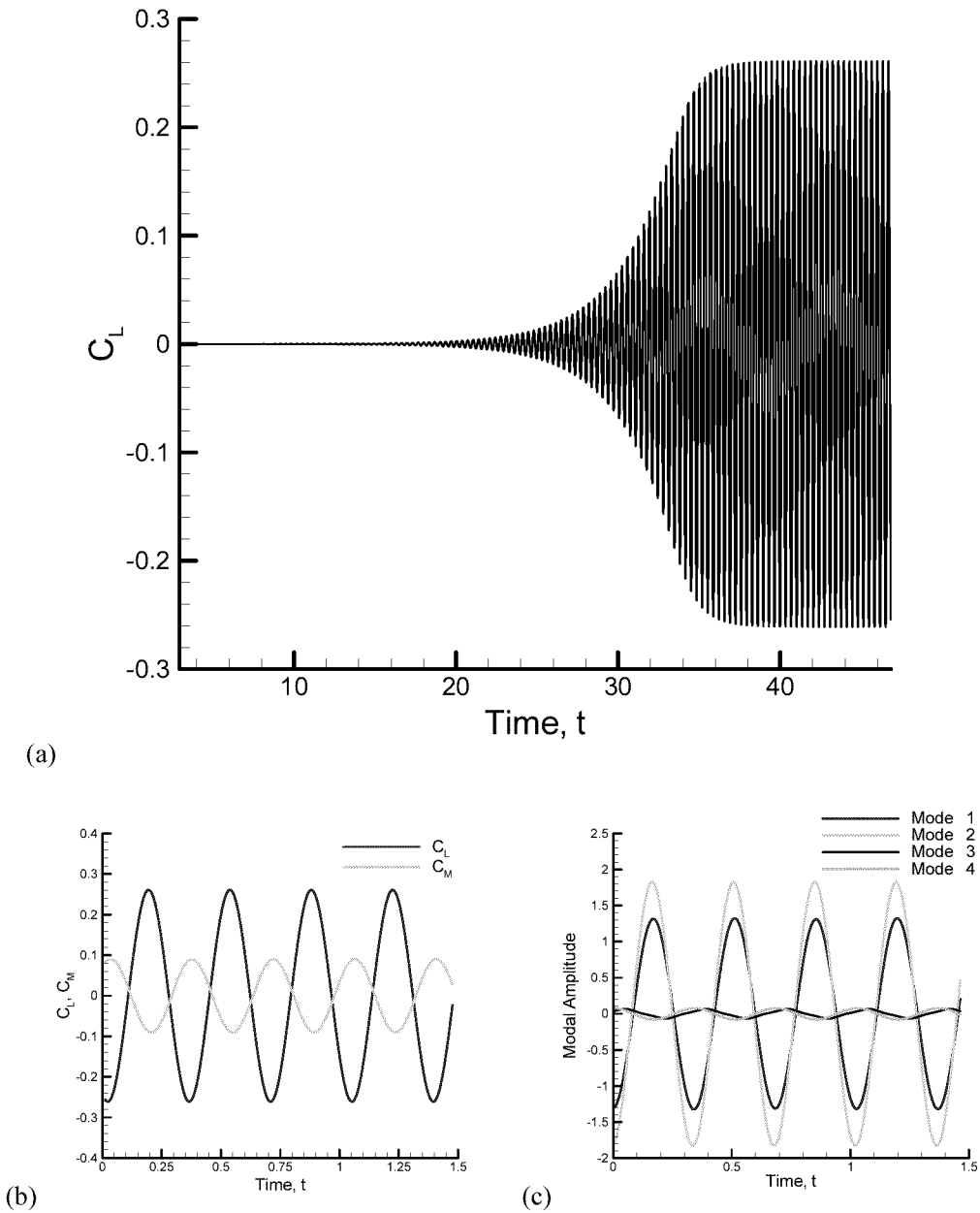
Figure 6: Inviscid CAPTSDv aeroelastic analysis for grid G1 without store aerodynamics at Mach 0.92 and $U = 410$ ft/sec: (a) time history of lift coefficient; (b) lift and moment coefficients at LCO; (c) modal amplitudes at LCO.

(a)

(b)

(c)
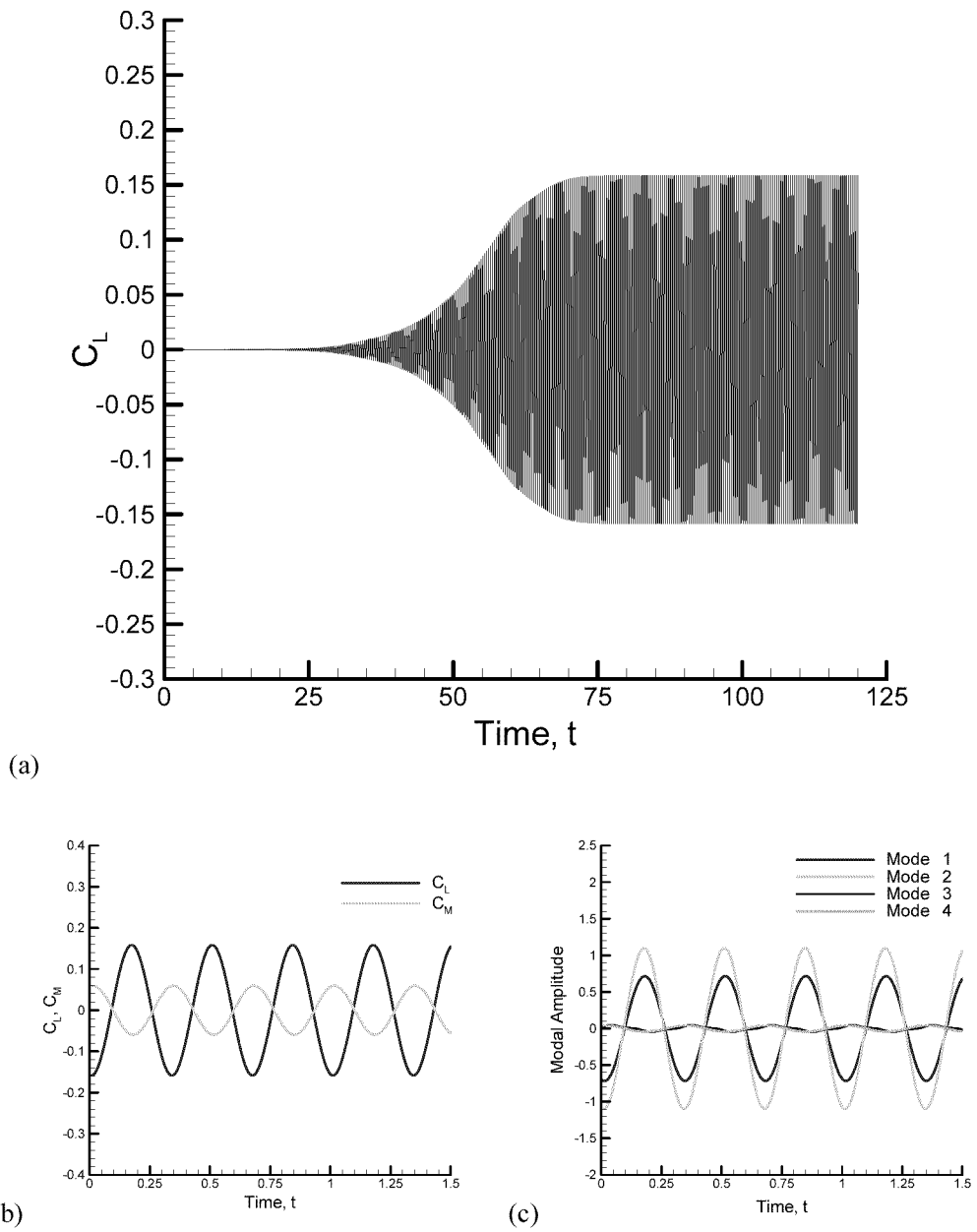
Figure 7: Viscous CAPTSDv aeroelastic analysis for grid G3 without store aerodynamics at Mach 0.92 and $U = 410$ ft/sec: (a) time history of lift coefficient; (b) lift and moment coefficients at LCO; (c) modal amplitudes at LCO.
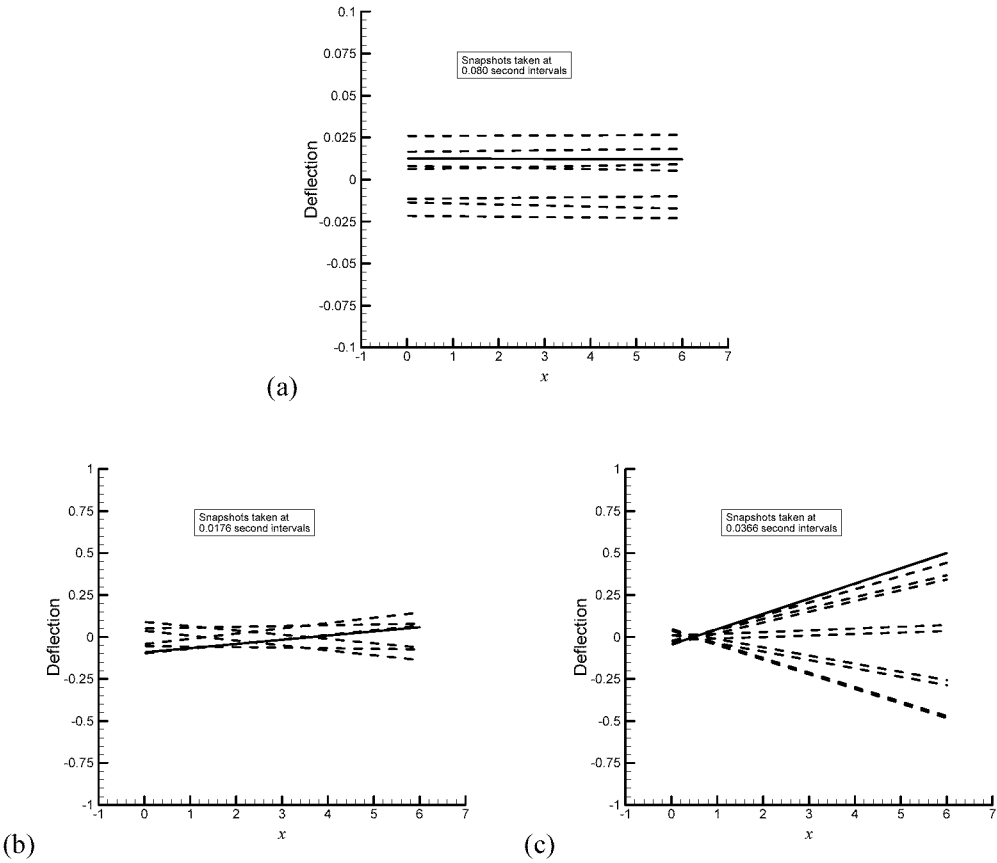
Figure 8: Snapshots of wingtip chordlines (G1) three characteristic aeroelastic responses: (a) flutter at Mach 0.84 ($U = 750$ ft/sec); (b) flutter at Mach 0.90 ($U = 850$ ft/sec); (c) LCO at Mach 0.92 ($U = 410$ ft/sec).
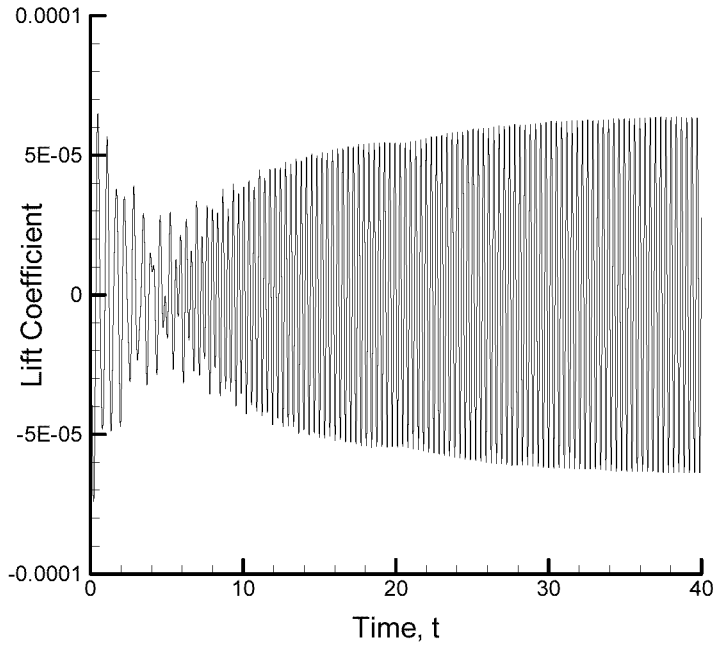
Figure 9: Low-amplitude oscillations at Mach 0.92 and $U = 385$ ft/sec (grid G1).
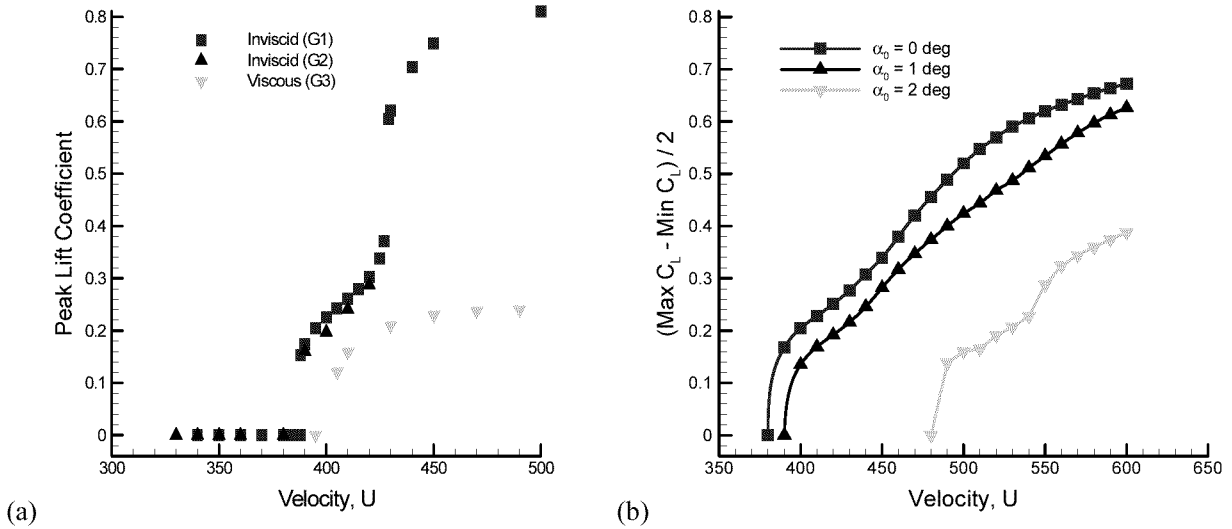
Figure 10: Comparison of LCO response boundaries for different CAPTSDv analyses: (a) inviscid analysis with (G2) and without (G1) inclusion of store aerodynamics, and viscous analysis (G3) for Mach 0.92; (b) inviscid analysis without store aerodynamics at selected angles of attack for Mach 0.93.
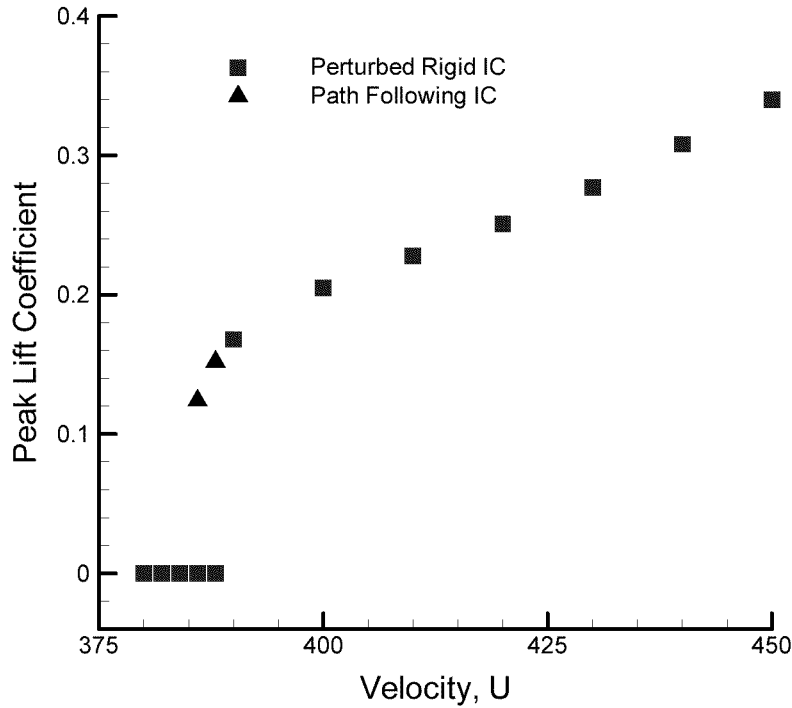

Figure 11: Demonstration of subcritical Hopf bifurcation and non-unique aeroelastic behavior at Mach 0.93 (wing/store model without store aerodynamics). Two initial conditions are employed: baseline initial conditions ("Perturbed Rigid IC") and converged LCO solutions at higher velocities ("Path Following IC").
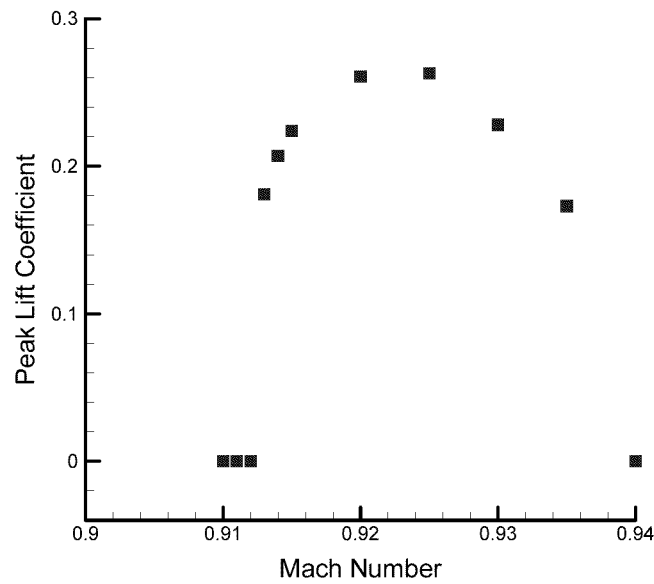
Figure 12: Variation of LCO response for different Mach numbers at U = 410 ft/sec (wing/store model without store aerodynamics).
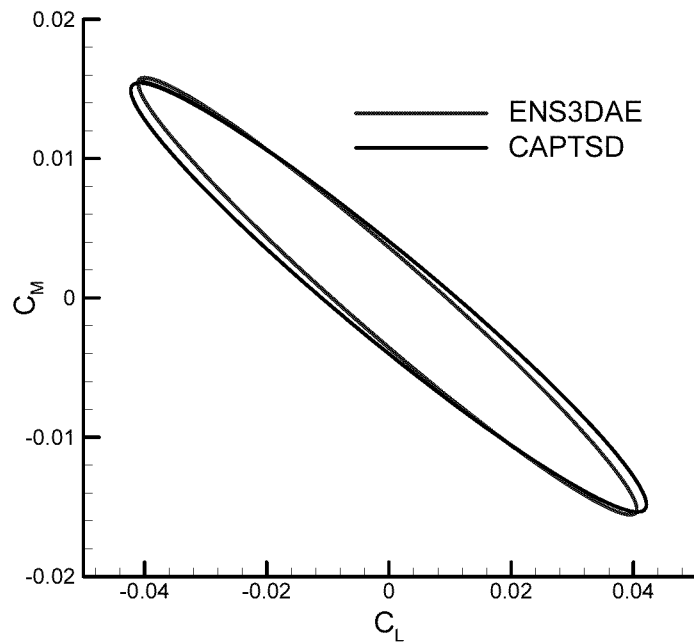

Figure 13: Comparison of C_L–C_M phase portraits predicted by CAPTSDv and ENS3DAE for forced pitch oscillation (amplitude of ½ deg at 3 Hz) of the rigid wing at Mach 0.92 and U = 400 ft/sec.